Icarus 396 (2023) 115493

Contents lists available at ScienceDirect

Icarus

journal homepage: www.elsevier.com/locate/icarus

Quantifying the effects of submicroscopic metallic iron on VIS–NIR spectra of lunar soils

Yanhua Peng[a,b,c], Siting Zhang[b,*], Hong Tang[b], Zhuang Guo[b,d], Wen Yu[b], Guozhu Chen[a], Chen Li[b], Bingkui Miao[a], Bing Mo[b], Encheng He[a,b], Ting Zhou[a,b], Zhipeng Xia[a], Lilin Huang[e]

[a] *Institution of Meteorites and Planetary Materials Research, Key Laboratory of Planetary Geological Evolution at Universities of Guangxi Province, Guilin University of Technology, Guilin 541004, China*
[b] *Center for Lunar and Planetary Sciences, Institute of Geochemistry, Chinese Academy of Sciences, Guiyang 550081, China*
[c] *Nanning College of Technology, Guilin 541006, China*
[d] *Institute of Remote Sensing and Geographical Information System, School of Earth and Space Sciences, Peking University, Beijing 100871, China*
[e] *Hezhou University, Hezhou 542899, China*

ARTICLE INFO

Keywords:
Moon
Surface
Airless bodies
Regolith
Spectroscopy

ABSTRACT

Metallic iron (Fe^0) particles with sizes ranging from a few nanometers to the submicroscopic scale and formed by space weathering are specific components of lunar soil. Previous studies have suggested that the iron significantly alters the optical properties of lunar soil. For example, nanophase metallic iron ($npFe^0$) causes both reddening and darkening of the lunar soil spectrum, and submicroscopic metallic iron (SMFe) only causes darkening. Here, we prepared SMFe particles with an average size of ~180 nm embedded within melt glasses through carbothermal reduction experiments to analogize agglutinated glasses in the lunar soil. We evaluated the effect of SMFe content on visible and near-infrared (VIS–NIR) reflectance spectra of these lunar soil samples simulants. The spectral data show that SMFe content plays a key role in the optical properties of samples, including the average reflectance in the VIS-NIR range (400–2150 nm), and the absorption depth at ~2 μm. A small amount (0.05 wt%) of SMFe mainly causes significant spectral darkening, and the average reflectance is reduced by 50% when the SMFe content rises to 0.36 wt%. Both the average reflectance and the absorption depth at ~2 μm show a negative correlation with the SMFe content. We developed a quantitative model relating the spectral characteristics and the SMFe abundance based on experimental results. Thus, the SMFe contents play a key role in altering spectral characteristics of airless bodies during remote sensing spectroscopic detection.

1. Introduction

Metallic iron (Fe^0) is a common phase in airless bodies such as the Moon, Mercury, and asteroids (Hapke, 2001). Lacking atmospheric protection, airless planets are directly exposed to the space environment and subjected to continuous high-velocity impacts from meteorites and micrometeorites and to steady bombardment from cosmic rays and solar-wind particles. These high-velocity impacts lead to physical and chemical changes in the surface materials, a process called space weathering (Anand et al., 2004; Heiken et al., 1991; Pieters and Noble, 2016). Physical changes caused by space weathering are breaking up of rocks into soil and chemical changes resulting in formation of new impact-induced Fe^0 particles or other iron-silicides in the lunar regolith (Anand et al., 2004). Mössbauer and magnetic analyses have found widely distributed Fe^0 particles in lunar samples (Huffman et al., 1974; Nagata et al., 1970; Pearce et al., 1972). Transmission electron microscopy (TEM) of lunar samples has provided a more intuitive understanding of Fe^0 particle distribution (Basu, 2005; Basu et al., 2001; Cymes et al., 2021; Pieters and Noble, 2016). Fe^0 in lunar samples is mainly found in the amorphous coating of grains (Noble et al., 2005) and the interior of agglutinates (Taylor and Taylor, 2009), which are typically spherical with particle sizes ranging from a few nanometers to hundreds of nanometers (Hapke, 2001). Fe^0 distributed in amorphous coating is typically nano-phase metallic iron ($npFe^0$) with an average particle size of 3 nm, while submicroscopic metallic iron (SMFe), with a particle size up to 1 μm, is mainly embedded within agglutinated glasses (Basu, 2005; Basu et al., 2001; Taylor and Taylor, 2009). A previous study found that agglutinated glasses form by remelting of the finest

---

* Corresponding author.
E-mail address: zhangsiting@mail.gyig.ac.cn (S. Zhang).

https://doi.org/10.1016/j.icarus.2023.115493
Received 30 December 2022; Received in revised form 13 February 2023; Accepted 14 February 2023

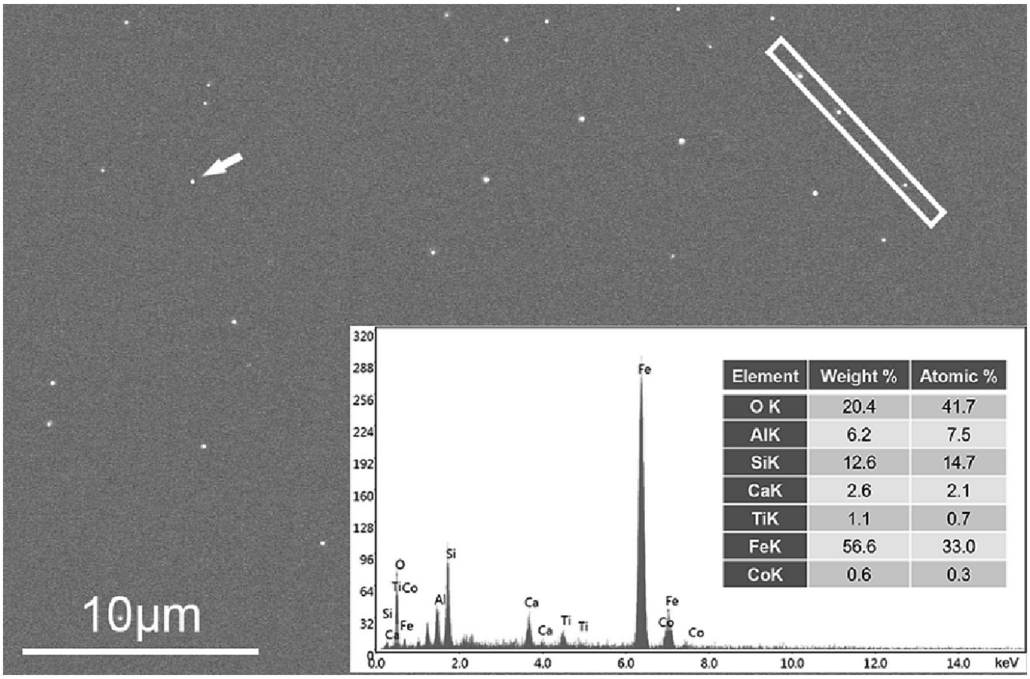

Element	Weight %	Atomic %
O K	20.4	41.7
AlK	6.2	7.5
SiK	12.6	14.7
CaK	2.6	2.1
TiK	1.1	0.7
FeK	56.6	33.0
CoK	0.6	0.3

Fig. 1. BSE image of a quenched sample prepared by the reduction reaction of graphite and CLRS-2. The EDS spectrum for the bright dot indicated by the white arrow is inserted into the bottom right corner of this image. The white rectangle shows the foil extraction locations of the focused ion beam (FIB) section.

fractions of lunar soils, and the Fe^0 particles tend to form larger particles during melting (Taylor et al., 2000).

Lunar soil has a lower reflectance, weaker absorption, and redder spectrum than lunar rock collected at the same sites (Adams and Jones, 1970; Adams and McCord, 1971; Conel and Nash, 1970; Hapke et al., 1970). Previous studies of spectral properties of lunar soils focused mainly on the effect of soil particle size and agglutinate content. Maturity is a measure of the time in which the soil is in the uppermost ~1 mm of the lunar surface (Morris, 1978). As the maturity of lunar soil increases, smaller grain size and higher agglutinate content (up to 60%) are observed (McKay et al., 1972). However, other studies suggest that optical alteration of lunar soil is not simply caused by mechanical fragmentation (Adams and Filice, 1967; Fischer and Pieters, 1994). Agglutinates have also been observed to be darker than the parent lunar soil, and increased agglutinate contents observed in the lunar soil spectrum also cause the soil to become darker (Adams and McCord, 1973). Cassidy and Hapke (1975) crushed Apollo samples that had been melted in vacuum and found that the spectra of the crushed agglutinate samples became brighter with stronger absorption bands rather than darker and redder. Therefore, agglutinate glasses are insufficient to fully account for lunar optical alteration (Cassidy and Hapke, 1975).

Further analysis of returned lunar samples has identified nano- to submicron-sized metallic iron in the lunar soil as the dominant factor in spectral changes (Keller and Mckay, 1993; Keller and McKay, 1997; Pieters and Noble, 2016). Studies have shown that the reddening of the lunar soil spectrum is mainly due to $npFe^0$, and SMFe particles mainly cause the spectral darkening and mask the spectral absorption features without reddening the spectrum (Allen et al., 1996; Lucey and Riner, 2011; Pieters and Noble, 2016; Pieters et al., 2000). Noble et al. (2007) conducted a more detailed investigation of the effect of Fe^0 particle size on lunar soil spectra. They prepared a series of analogs containing Fe^0 grains with different sizes and abundances by reducing silica gel with different pore sizes. Their results showed that $npFe^0$ particles with smaller diameters (<10 nm) lowered the reflectance throughout the visible-near-infrared (VIS–NIR) range and significantly reddened the spectrum in the VIS band. SMFe particles with larger diameters (>40 nm) darken the spectrum in the VIS–NIR band and very slightly change the shape of the continuum. In addition to experiments, several numerical models (Escobar-Cerezo et al., 2018; Hapke, 2001; Lucey and Noble, 2008) also suggest that SMFe particles darken the spectrum. In addition to the Moon, SMFe is equally important for our understanding of other unlanded airless bodies in the solar system, such as Mercury and Vesta, mainly because these bodies tend to be dominated by dark features causes by space weathering processes (Pieters et al., 2012).

Various evaluations of the effects of particle size and impacted-glass content on optical properties have confirmed the important role of SMFe in lunar soil. However, although nanophase iron particles have been studied in depth, there are not enough studies on the effect of SMFe on lunar soil spectra, especially the quantitative effect of SMFe abundance. In this study, we quantify the relationship between SMFe abundance and reflectance by investigating the VIS–NIR spectra of simulant samples with different SMFe contents.

2. Sample and analytical techniques

2.1. Sample preparation

In this study, iron-containing materials were prepared from lunar soil simulant by high-temperature reduction. The sample preparation was as follows. (1) The raw materials were industrial graphite and CLRS-2 (high-Ti Chinese lunar regolith simulant, from the same series as CLRS-1) (Tang et al., 2017; Zheng et al., 2009). CLRS-2 is mainly

Table 1
Composition of the glass before magnetic sorting measured by XRF (wt%).

Chemical composition	SiO_2	Fe_2O_3	Al_2O_3	CaO	MgO	TiO_2	Na_2O	MnO	K_2O	P_2O_5
Content (wt%)	37.37	1.80	32.38	9.75	7.28	6.49	2.24	0.20	0.72	0.02

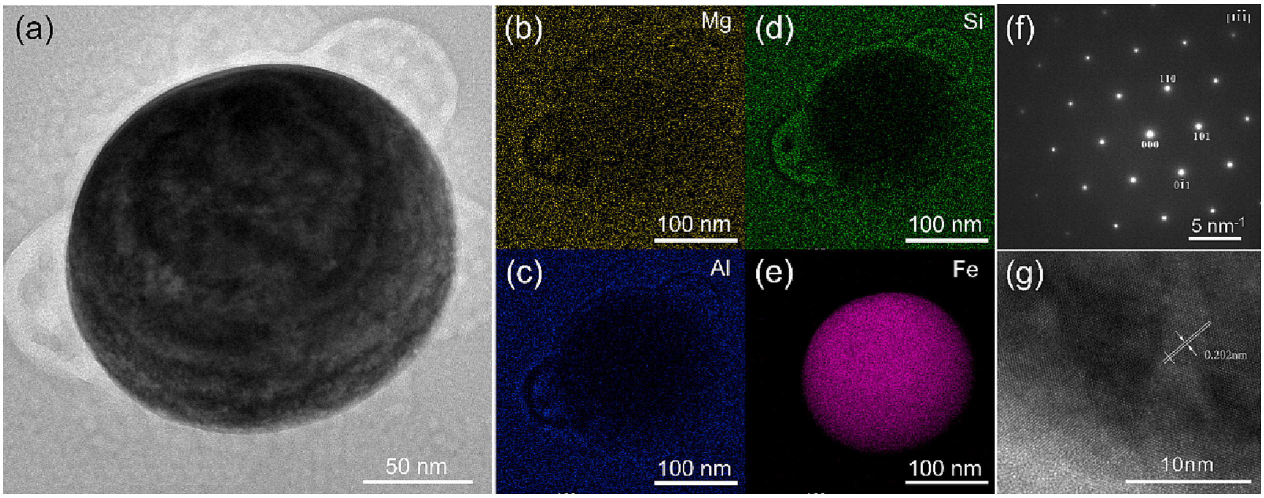

Fig. 2. (a) Bright-field image of part of the foil extracted using the FIB, showing a close view of a Fe^0 particle. (b–e) EDS maps for the four main elements of Fe^0 in (a): Mg, Al, Si, and Fe. (f–g) Selected-area electron diffraction (SAED) patterns and high-resolution TEM image of Fe^0 in (a).

composed of volcanic glass, pyroxene, olivine, and feldspar, and its elemental composition has been reported in past work (Peng et al., 2022). Graphite and CLRS-2 were mixed with a mass ratio of 1:27 and put into a high-purity corundum crucible. (2) The mixture was heated at 1600 °C for 4 h in argon gas as a protective environment, in which SMFe does not oxidize. After heating at 1600 °C for 4 h, all the minerals melted completely, and iron species were reduced by graphite and formed metallic iron. (3) The melted samples were quenched with water. The quenched glass contained a large amount of reduced Fe^0 particles (Fig. 1). The glass composition is shown in Table 1. (4) The quenched glass was crushed into powder using a planetary ball mill, and the powder particle size was <20 μm. (5) The powder was put into a magnetic sorter, divided into magnetic (MAG, with metallic iron) and non-magnetic (non-MAG, without metallic iron) fractions, and used to prepare samples with different SMFe abundances.

2.2. Analytical techniques

Before crushing the quenched samples, we cut ~15 mm × 45 mm sections and polished them for microscopic observation. We examined sample morphology via backscattered electron (BSE) imaging and conducted semi-quantitative analysis via energy dispersive X-ray spectrometry (EDS) using a scanning electron microscope (SEM) at the Lunar and Planetary Science Research Centre, Institute of Geochemistry, CAS. The high-resolution BSE imaging and EDS analysis were performed at an accelerating voltage of 15 kV. The morphology and microstructure were studied with an FEI Scios dual-beam focused ion beam-scanning electron microscope (FIB-SEM) and transmission electron microscope (TEM). TEM lamellae were prepared using the FIB processing capability of the dual-beam scanning electron microscope, and were subsequently characterized using an FEI Talos F200S field-emission scanning transmission electron microscope (FE-STEM) equipped with an EDS detector at Guangdong University of Technology. We obtained EDS maps using the STEM to understand the nanometer-scale chemical composition of the TEM samples, and identified the crystal structure of the nanoscale phases through high-resolution (HR) TEM images and selected-area electron diffraction (SAED) maps.

To obtain the Fe^0 content in MAG and non-MAG fractions, an Agilent Technologies inductively coupled plasma optical emission spectrometer (ICP-OES) was used to determine the total iron content in our samples.

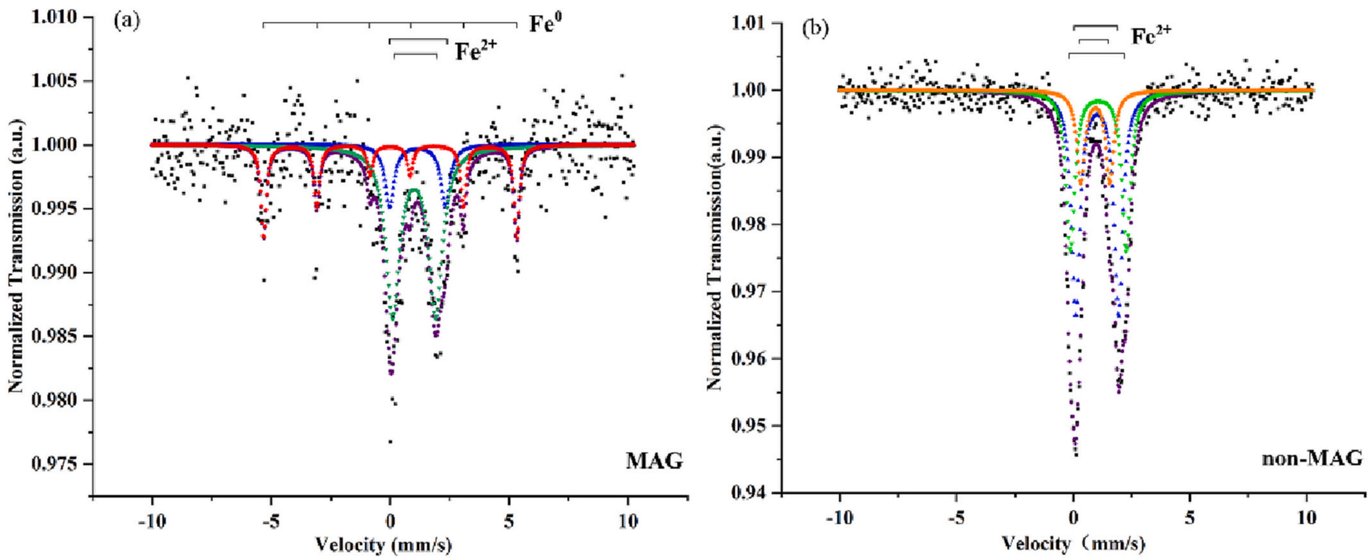

Fig. 3. ^{57}Fe resonant absorption Mössbauer spectra of the samples. (a) Magnetic fraction after magnetic separation (MAG) and (b) non-magnetic fraction after magnetic separation (non-MAG). The red subspectrum for MAG corresponds to Fe^0, and the non-MAG subspectra all show ferrous iron. No Fe^0 signal is detected.

Table 2
Compositions of samples with different Fe^0 abundances.

Sample	Fe^0 (wt%)	Mixing ratios (wt%)	
		MAG	non-MAG
1	0.00	0.00	100.00
2	0.05	13.89	86.11
3	0.10	27.78	72.22
4	0.15	41.67	58.33
5	0.18	50.00	50.00
6	0.20	55.56	44.44
7	0.25	69.44	30.56
8	0.30	83.33	16.67
9	0.36	100.00	0.00

Then, the Fe^0 content of the total iron of each sample was analyzed using iron Mössbauer spectroscopy (FeMS). Finally, the Fe^0 content in the samples was directly calculated. The ICP-OES analysis was performed at the State Key Laboratory of Mineral Deposit Geochemistry, Institute of Geochemistry, Chinese Academy of Sciences (CAS), on an Agilent Technologies instrument. The Fe^0 content of the total iron in each powder sample was collected with an MFD-500AV (Topologic·Japan) iron Mössbauer Spectrometer at the Center for Advanced Mössbauer Spectroscopy, Dalian Institute of Chemical Physics, CAS. The Mössbauer spectra were collected at a room temperature of 298 K and a humidity of 15% using a ^{57}Co single-line source embedded in Rh for a run time of 24 h.

The visible to near-infrared spectra were obtained at the Institute of Geochemistry, CAS, using a Cary 500 UV–VIS–NIR spectrophotometer equipped with an integrating sphere. Each VIS–NIR spectrum was recorded as a percentage of reflectance (R%). For each sample, three measurements were taken and averaged to ensure that the obtained spectra of each sample were as accurate as possible.

3. Results

3.1. Microscopic observations

The BSE image shows a lot of bright spots distributed in the samples (Fig. 1). The EDS result shows that these small bright dots are rich in iron. Studies have shown that the Fe^0 within lunar soil is α-Fe with body-centered cubic (bcc) structure (Liu et al., 2007; Thompson et al., 2016). To identify the crystal structure of the bright dots in the product, the TEM sample was extracted with FIB methods from the position of the white rectangle on the right in Fig. 1. The TEM results are shown below.

Fig. 2 shows TEM images and EDS maps of the foil. It is clear that the metallic iron has a diameter of approximately 180 nm (Fig. 2a). In a previous study (Peng et al., 2022), we measured a number of particles in the range 40–200 nm with an average size of 180 ± 10 nm. TEM X-ray EDS maps show that these Fe^0 particles are essentially elemental iron and contain no significant Mg, Si, or O (Fig. 2b–e). The SAED patterns (Fig. 2f–g) show that these Fe^0 particles are α-Fe (Im3m space group with a lattice plane distance of 0.202 nm). Therefore, α-Fe is present in quenched glass reduced by CLRS-2.

3.2. Mössbauer spectroscopy and ICP-OES analysis

As shown in Fig. 3, the MAG fractions were found to have a distinct α-Fe spectrum, and no α-Fe spectra were observed in the non-MAG. The Fe^0 contents of the MAG and non-MAG are 0.36 wt% and 0 wt%, respectively, on the basis of FeMS and ICP-OES results. Subsequently, we mixed the MAG and non-MAG in different proportions to obtain a group of samples with different iron abundances (Table 2). Here, the Fe^0 particles are contained in the glass, which is similar to the Fe^0 in agglutinates of lunar soils.

3.3. Reflectance spectra

The reflectance spectra of samples with different SMFe abundances are shown in Fig. 4a, and the same spectra normalized at 450 nm are shown in Fig. 4b. Because these spectra show significant noise at longer wavelengths, this study takes the 400–2150 nm band for further analysis to reduce the effect of noise on the spectral shape. All samples show a monotonic increase at shorter wavelengths (400–1400 nm) and become relatively stable at longer wavelength (>1400 nm), with a broad weak absorption band near 2 μm. In general, the reflectance spectra show three distinct trends with increasing SMFe abundance: (1) The spectral reflectance increases nearly linearly in the visible portion of the spectrum (450–780 nm). (2) The spectrum gradually darkens throughout the whole wavelength range (400–2150 nm) with increasing SMFe abundance. (3) The absorption band depth slightly weakens at ~2 μm. More detailed spectral characteristics are described next.

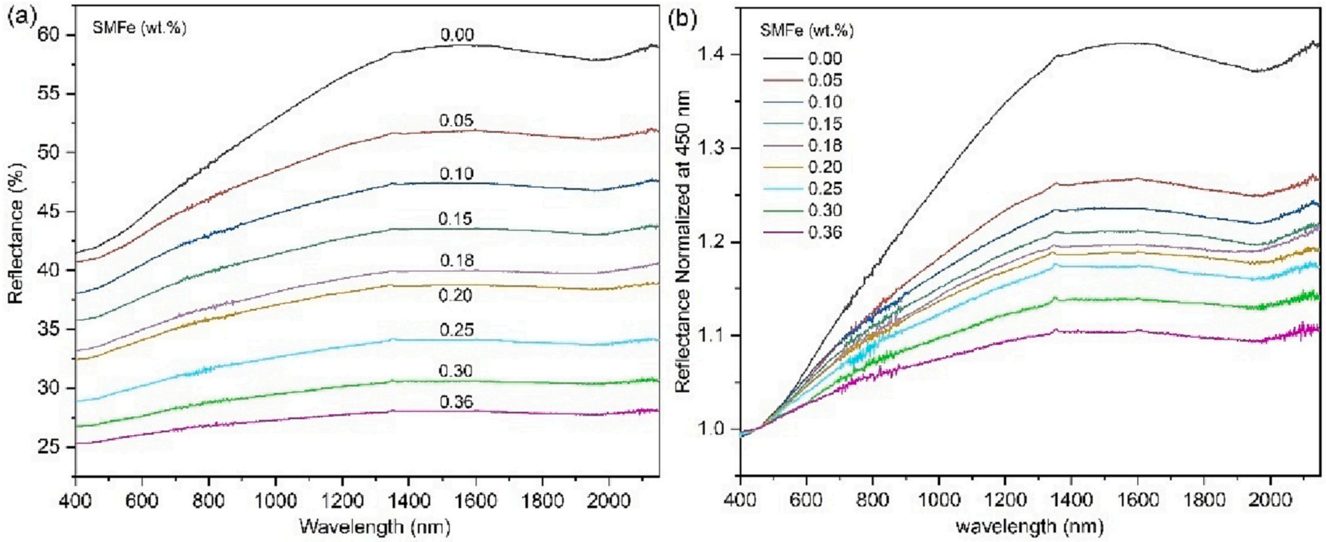

Fig. 4. (a) VIS–NIR reflectance spectra of samples with different SMFe abundances and (b) reflectance spectra normalized at 450 nm. The sample containing no iron (0.00 wt%) corresponds to non-MAG.

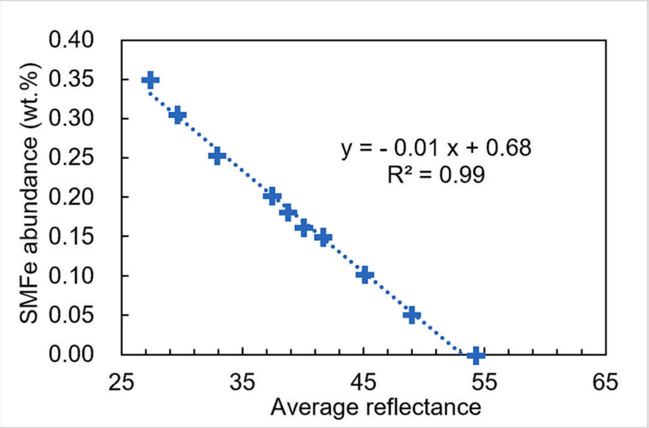

Fig. 5. Correlation of the average reflectance in the 400–2150 nm band with SMFe abundance.

4. Discussion

4.1. *Effects of SMFe abundance on reflectance spectra*

The sample with low SMFe abundance (0.05 wt%) shows a significant decrease in reflectance relative to the original sample (0 wt% SMFe) (Fig. 4a). As SMFe increases, the rate of reflectance reduction becomes slower but is not simply linear. When the SMFe abundance goes up to 0.36 wt%, the overall reflectance decreases by ~50% compared with that of the original sample. The variation of the spectra with SMFe content indicates a significant effect of SMFe on reflectance reduction. This is consistent with the laboratory study of Noble et al. (2007) on silica gel powder containing SMFe. In their study, a SG50 suite with grain sizes of 30–75 μm showed a darker spectrum than a SG2 suite with grain sizes of 125–250 μm. This was when the SMFe contents were the same in the SG50 and SG2 suites with particle sizes of 20–200 nm and 5–15 nm, respectively. Because larger particles usually have a lower reflectance than smaller ones (Adams and Filice, 1967), those authors attributed the spectral darkening to the increase in SMFe particle size. Agglutinitic glass is a major product of space weathering, up to ~70% of lunar soil (Liu and Taylor, 2011). Thus, we conclude that SMFe, a major component of agglutinate glass, is one of the major factors darkening the lunar soil spectrum.

Besides the Moon, the space weathering product SMFe is predicted to be one of the main factors altering optical properties on Mercury (Lucey and Riner, 2011). In fact, there is still no consensus on the darkening agent on Mercury. Crustal-sourced carbon (graphite) has been proposed to be the darkening agent on Mercury because of its low iron content and the low albedo material typically found in large impact craters and their ejecta (Murchie et al., 2008; Peplowski et al., 2016; Solomon et al., 2018; Vander Kaaden and McCubbin, 2015). However, although the iron content of Mercury's surface is significantly lower than that of the Moon, only a small fraction of iron on the Moon is reduced by space weathering (Keller et al., 1999; Morris, 1980), whereas almost all of the iron on Mercury is reduced (Noble and Pieters, 2003). Noble and Pieters (2003) suggested that even in the extreme case of the absence of native iron on the surface of Mercury, the iron brought by meteorites should be sufficient to affect optical properties. Moreover, because Mercury is closer to the Sun and has more mass, the temperature, impactor velocity, and flux are greatly increased (Cintala, 1992; Marchi et al., 2009; Noble et al., 2007). At high velocities, high fluxes, and high temperatures, soil particles are repeatedly impacted and melted and coalesced, which helps npFe^0 grow into SMFe. Not only does the model of Lucey and Riner (2011) show that Mercury has a high ratio of SMFe to npFe^0 (higher than the Moon), but the model of Trang et al. (2015) also has the best spectral matches in terms of Fe^0 and carbon in the nanophase and iron in microphase particles in combination.

4.2. *Quantitative analysis of the effect of SMFe abundance on reflectance spectra*

The reflectance spectra in Fig. 4 show regular variation with increasing SMFe abundance. As SMFe increases, the reflectance decreases, the slope becomes less red, and the characteristic absorption band weakens. Therefore, to clarify the quantitative relationship between the reflectance and SMFe abundance, we tried to establish a regression equation for the average reflectance of the whole band (400–2150 nm) and SMFe abundance. We also investigated the relationship between SMFe abundance and the absorption depth at ~2 μm.

4.2.1. *Correlation between SMFe abundance and average reflectance*

As seen in Fig. 5, the reflectance of the spectra decreases with increasing SMFe. We defined the average reflectance over the whole band (400–2150 nm) as the average reflectance. Using the SMFe distribution and the corresponding average reflectance, we tentatively determined that the relationship between SMFe abundance and average reflectance was consistent with the primary function $y = ax + b$, where x is the reflectance, and y is the corresponding SMFe abundance. The coefficient of determination R^2 is as high as 0.99. The results suggest that SMFe has a significant effect on the spectral reflectance, which is consistent with numerical models (Lucey and Noble, 2008; Lucey and Riner, 2011; Penttilä et al., 2020). Therefore, we conclude that the SMFe abundance and the average reflectance of the samples have a good negative linear relationship.

4.2.2. *Correlation between SMFe abundance and absorption depth at ~ 2 μm*

Absorption depth is the degree of reduction in reflectance of the absorbing region relative to that of the adjacent non-absorbing region in the VIS–NIR spectrum. As mentioned earlier, the shape of the reflectance spectrum of a lunar sample reflects its chemical and mineralogical composition. The diagnostic absorption bands at 2 μm are mainly dominated by Fe^{2+} (Tompkins and Pieters, 2010), and the absorption band can be weakened by space-weathering-reduced Fe^0 particles (Pieters and Fischer, 1993). All samples here have the same Fe^{2+} content. Here, we try to establish the relationship between SMFe and absorption depth at ~2 μm. The absorption depth is defined as the distance between the lowest point of the absorption valley in the vertical direction and the straight line connecting the left and right shoulders. We assume that the linear equation connecting the left and right shoulders of the absorption valley is.

$$f(\lambda) = \mathrm{a}\lambda + \mathrm{b} \tag{1}$$

where a and b are constant, λ is the wavelength, and $f(\lambda)$ is the corresponding reflectance. The absorption depth D of the spectrum is then expressed as.

$$\mathrm{D} = f(\lambda_{est}) - R_{est} \tag{2}$$

where λ_{est} is the wavelength of the lowest point of the absorption valley, and R_{est} is the reflectance of the lowest point of the absorption valley.

If the wavelengths and reflectances of the left and right shoulders and the lowest point of the absorption valley are all known, then according to Eqs. (1) and (2), the absorption depth D is

$$D = \frac{R_r - R_l}{\lambda_r - \lambda_l}\lambda_{est} + \frac{R_l\lambda_r - R_r\lambda_l}{\lambda_r - \lambda_l} - R_{est} \tag{3}$$

where λ_r, λ_l, and λ_{est} are the wavelengths of the right shoulder, left shoulder, and lowest point of the absorption valley, respectively; and R_r, R_l, and R_{est} are the reflectances of the right shoulder, left shoulder, and lowest point of the absorption valley, respectively.

The absorption depth of the spectrum varies regularly with the SMFe

Table 3
Characteristics of absorption valleys of samples with different SMFe contents.

Content (SMFe wt %)	Left shoulder		Lowest point		Rigth shoulder		Depth
	λ (μm)	R (%)	λ (μm)	R (%)	λ (μm)	R (%)	
0.00	1.603	59.129	1.962	57.873	2.126	59.204	1.308
0.05	1.599	51.952	1.955	51.164	2.127	52.103	0.890
0.10	1.602	47.431	1.956	46.814	2.130	47.764	0.841
0.15	1.601	43.585	1.950	43.032	2.130	43.876	0.745
0.18	1.600	40.011	1.948	39.745	2.135	40.593	0.645
0.20	1.600	38.799	1.966	38.405	2.129	38.939	0.491
0.25	1.596	34.110	1.959	33.714	2.116	34.221	0.474
0.30	1.598	30.616	1.950	30.354	2.130	30.871	0.431
0.36	1.601	28.076	1.953	27.737	2.124	28.109	0.361

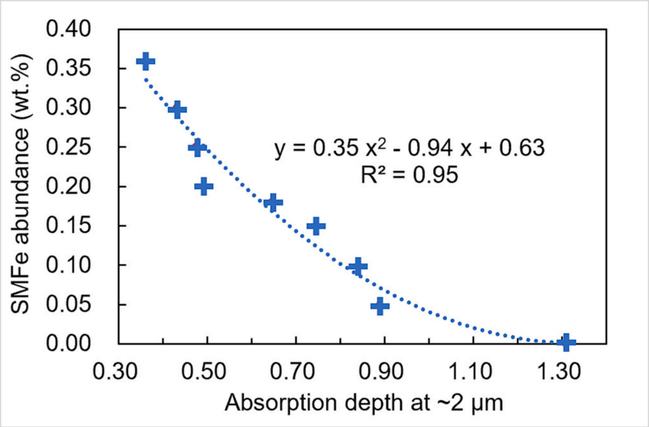

Fig. 6. SMFe abundance versus absorption band depth at ~2 μm.

abundance (Table 3). Fig. 6 shows the relationship between the SMFe abundance and the absorption depth at ~2 μm. Here, x is the absorption depth, and y is the corresponding SMFe abundance. As the corresponding absorption depth increases, the SMFe abundance decreases overall, which is consistent with the expectation that SMFe will weaken the absorption depth. The absorption depth at ~2 μm correlates very well with SMFe abundance with $R^2 \sim 0.95$. These results indicate that the absorption depth is mainly influenced by metallic iron even though it is influenced by other factors such as particle size, iron ion abundance, and site symmetry (Tompkins and Pieters, 2010). Thus, our results show that the absorption depth at ~2 μm has a good negative correlation with the SMFe abundance.

5. Conclusions

In this study, the SMFe particles were prepared by high-temperature carbothermal reduction of lunar soil simulants. We identified SMFe production through electron microscopy, and the iron particle size was in the range 40–200 nm with an average size of ~180 nm. The reduced SMFe particles were contained in glassy material, which is similar to the SMFe distribution of agglutinitic glass in lunar soil. The resulting reflectance spectra for different SMFe abundances suggest that SMFe strongly affects the VIS–NIR spectrum. The average reflectance of the sample containing 0.05 wt% SMFe decreased by ~9.0% compared with that of the sample without SMFe. When SMFe content reaches 0.36 wt%, the average reflectance decreases by ~50%. In addition to causing spectral darkening, SMFe contributes to weakening the characteristic absorption. Therefore, the present study is important for understanding the composition and evolution of airless bodies (e.g., the Moon, Mercury, and Vesta) through remote sensing. The correlation analysis shows that the average reflectance of the VIS–NIR spectrum and the absorption depth at approximately 2 μm correlate highly with SMFe abundance. Furthermore, the average reflectance and the absorption depth of the VIS–NIR spectrum can be used to estimate the metallic iron content of lunar soil.

Declaration of Competing Interest

None.

Data availability

Data will be made available on request.

Acknowledgements

We acknowledge the help of Chuanjiao Zhou and Rui Li in spectral measurements. Thanks go to Yang Li for helpful comments during the production of this manuscript. This work was supported by the Strategic Priority Research Program of the Chinese Academy of Sciences (CAS) (XDB 41000000); National Natural Science Foundation of China (42263005); Guangxi University Young and Middle-aged Teachers' Basic Scientific Research Ability Improvement Project (No. 2020KY58009); and Guangxi Scientific Base and Talent Special Projects (AD22035157).

References

Adams, J.B., Filice, A.L., 1967. Spectral reflectance 0.4 to 2.0 microns of silicate rock powders. J. Geophys. Res. 72 (22), 5705–5715. https://doi.org/10.1029/JZ072i022p05705.

Adams, J.B., Jones, R.L., 1970. Spectral reflectivity of lunar samples. Science 167 (3918), 737–739. https://doi.org/10.1126/science.167.3918.737.

Adams, J.B., McCord, T.B., 1971. Alteration of lunar optical properties: age and composition effects. Science 171 (3971), 567–571. https://doi.org/10.1126/science.171.3971.567.

Adams, J.B., McCord, T.B., 1973. Vitrification darkening in the lunar highlands and identification of Descartes material at the Apollo 16 site. In: Lunar and Planetary Science Conference Proceedings, p. 163.

Allen, C., Morris, R., McKay, D., 1996. An experimental analog to maturing lunar soil. Lunar Plan. Sci. Conf. 13–14.

Anand, M., Taylor, L.A., Nazarov, M.A., Shu, J., Mao, H.-K., Hemley, R.J., 2004. Space weathering on airless planetary bodies: clues from the lunar mineral hapkeite. Proc. Natl. Acad. Sci. 101 (18), 6847–6851. https://doi.org/10.1073/pnas.0401565101.

Basu, A., 2005. Nanophase Fe0 in lunar soils. J. Earth Syst. Sci. 114 (3), 375–380.

Basu, A., Wentworth, S.J., Mckay, D.S., 2001. Occurrence and Distribution of Feo-Globules in Lunar Agglutinates, 2001. Lunar and Planetary Science XXXII.

Cassidy, W., Hapke, B., 1975. Effects of darkening processes on surfaces of airless bodies. Icarus 25 (3), 371–383. https://doi.org/10.1016/0019-1035(75)90002-0.

Cintala, M.J., 1992. Impact-induced thermal effects in the lunar and Mercurian regoliths. J. Geophys. Res. Planets 97 (E1), 947–973.

Conel, J., Nash, D., 1970. Spectral reflectance and albedo of Apollo 11 lunar samples: effects of irradiation and vitrification and comparison with telescopic observations. Geochimica et Cosmochimica Acta Supplement 1, 2013.

Cymes, B., Burgess, K., Stroud, R., 2021. STEM-EELS-EDS analysis of space weathering features of ANGSA lunar soil samples. Microsc. Microanal. 27 (S1), 2044–2046 doi:10.17/S143192762100742X.

Escobar-Cerezo, J., Penttilä, A., Kohout, T., Muñoz, O., Moreno, F., Muinonen, K., 2018. Simulations of effects of nanophase iron space weather products on lunar regolith reflectance spectra. Astrophys. J. 853 (1), 71. https://doi.org/10.3847/1538-4357/aaa24d.

Fischer, E.M., Pieters, C.M., 1994. Remote determination of exposure degree and Iron concentration of lunar soils using VIS-NIR spectroscopic methods. Icarus 111 (2), 475–488. https://doi.org/10.1006/icar.1994.1158.

Hapke, B., 2001. Space weathering from mercury to the asteroid belt. J. Geophys. Res. Planets 106 (E5), 10039–10073. https://doi.org/10.1029/2000JE001338.

Hapke, B., Cohen, A., Cassidy, W., Wells, E., 1970. Solar radiation effects on the optical properties of Apollo 11 samples. Geochimica et Cosmochimica Acta Supplement 1, 2199 https://doi.org/19700065544.

Heiken, G.H., Vaniman, D.T., French, B.M., 1991. Lunar Sourcebook : A User's Guide to the Moon.

Huffman, G., Schwerer, F., Fisher, R., Nagata, T., 1974. Iron distributions and metallic-ferrous ratios for Apollo lunar samples-Mossbauer and magnetic analyses. In: Lunar and Planetary Science Conference Proceedings, pp. 2779–2794.

Keller, L.P., Mckay, D.S., 1993. Discovery of vapor deposits in the lunar regolith. Science 261 (5126), 1305–1307. https://doi.org/10.1126/science.261.5126.1305.

Keller, L.P., McKay, D.S., 1997. The nature and origin of rims on lunar soil grains. Geochim. Cosmochim. Acta 61 (11), 2331–2341. https://doi.org/10.1016/S0016-7037(97)00085-9.

Keller, L.P., Wentworth, S.J., Gezo, J., McKay, D.S., Taylor, L.A., Pieters, C., Morris, R.V., 1999. Space weathering alteration of lunar soil grains. Lunar Plan. Sci. Conf. 1820.

Liu, Y., Taylor, L.A., 2011. Characterization of lunar dust and a synopsis of available lunar simulants. Planet. Space Sci. 59 (14), 1769–1783. https://doi.org/10.1016/j.pss.2010.11.007.

Liu, Y., Taylor, L.A., Thompson, J.R., Schnare, D.W., Park, J.S., 2007. Unique properties of lunar impact glass: nanophase metallic Fe synthesis. Am. Mineral. 92 (8–9), 1420–1427. https://doi.org/10.2138/am.2007.2333.

Lucey, P., Noble, S., 2008. Experimental test of a radiative transfer model of the optical effects of space weathering. Icarus 197 (1), 348–353. https://doi.org/10.1016/j.icarus.2008.05.008.

Lucey, P.G., Riner, M.A., 2011. The optical effects of small iron particles that darken but do not redden: evidence of intense space weathering on mercury. Icarus 212 (2), 451–462. https://doi.org/10.1016/j.icarus.2011.01.022.

Marchi, S., Mottola, S., Cremonese, G., Massironi, M., Martellato, E., 2009. A new chronology for the moon and mercury. Astron. J. 137 (6), 4936.

McKay, D.S., Heiken, G.H., Taylor, R.M., Clanton, U.S., Morrison, D.A., Ladle, G.H., 1972. Apollo 14 soils: size distribution and particle types. In: Lunar and Planetary Science Conference Proceedings, p. 983.

Morris, R.V., 1978. The surface exposure (maturity) of lunar soils: some concepts and Is/FeO compilation. In: Paper presented at the 9th Lunar and Planetary Science Conference.

Morris, R.V., 1980. Origins and size distribution of metallic iron in the lunar regolith. In: Lunar and Planetary Science Conference, pp. 747–749.

Murchie, S.L., Watters, T.R., Robinson, M.S., Head, J.W., Strom, R.G., Chapman, C.R., Solomon, S.C., McClintock, W.E., Prockter, L.M., Domingue, D.L., 2008. Geology of the Caloris basin, mercury: a view from MESSENGER. Science 321 (5885), 73–76.

Nagata, T., Ishikawa, Y., Kinoshita, H., Kono, M., Syono, Y., Fisher, R., 1970. Magnetic properties and natural remanent magnetization of lunar materials. Geochimica et Cosmochimica Acta Supplement 1, 2325–2340.

Noble, S., Pieters, C., 2003. Space weathering on mercury: implications for remote sensing. Sol. Syst. Res. 37 (1).

Noble, S., Keller, L., Pieters, C., 2005. Evidence of space weathering in regolith breccias I lunar regolith breccias. Meteorit. Planet. Sci. https://doi.org/10.1111/j.1945-5100.2005.tb00390.x.

Noble, S., Pieters, C., Keller, L., 2007. An experimental approach to understanding the optical effects of space weathering. Icarus 192 (2), 629–642. https://doi.org/10.1016/j.icarus.2007.07.021.

Pearce, G., Williams, R.J., McKay, D.S., 1972. The magnetic properties and morphology of metallic iron produced by subsolidus reduction of synthetic Apollo 11 composition glasses. Earth Planet. Sci. Lett. 17 (1), 95–104. https://doi.org/10.1016/0012-821X(72)90263-4.

Peng, Y., Tang, H., Mo, B., Zeng, X., Miao, B., 2022. Influencing factors for the preparation of Fe0 in lunar soil simulant using high-temperature carbothermic reduction. Adv. Space Res. 70 (10), 3220–3230. https://doi.org/10.1016/j.asr.2022.07.074.

Penttilä, A., Väisänen, T., Markkanen, J., Martikainen, J., Muinonen, K., 2020. Rigorous light-scattering simulations of nanophase iron space-weathering effects on reflectance spectra of olivine grains. Icarus 345, 113727.

Peplowski, P.N., Klima, R.L., Lawrence, D.J., Ernst, C.M., Denevi, B.W., Frank, E.A., Goldsten, J.O., Murchie, S.L., Nittler, L.R., Solomon, S.C., 2016. Remote sensing evidence for an ancient carbon-bearing crust on mercury. Nat. Geosci. 9 (4), 273–276.

Pieters, C.M., Fischer, E.M., 1993. Optical effects of space weathering: the role of the finest fraction. J. Geophys. Res. 98 (20), 20817–20824. https://doi.org/10.1029/93JE02467.

Pieters, C.M., Noble, S.K., 2016. Space weathering on airless bodies. J. Geophys. Res. Plan. 121 (10) https://doi.org/10.1002/2016JE005128.

Pieters, C.M., Taylor, L.A., Noble, S.K., Keller, L.P., Hapke, B., Morris, R.V., Allen, C.C., McKay, D.S., Wentworth, S., 2000. Space weathering on airless bodies: resolving a mystery with lunar samples. Meteorit. Planet. Sci. 35 (5), 1101–1107.

Pieters, C., Ammannito, E., Blewett, D., Denevi, B., De Sanctis, M., Gaffey, M., Le Corre, L., Li, J.-Y., Marchi, S., McCord, T., 2012. Distinctive space weathering on Vesta from regolith mixing processes. Nature 491 (7422), 79–82. https://doi.org/10.1038/nature11534.

Solomon, S.C., Nittler, L.R., Anderson, B.J., 2018. Mercury: The View after Messenger, 21. Cambridge University Press.

Tang, H., Li, X., Zhang, S., Wang, S., Liu, J., Li, S., Li, Y., Wu, Y., 2017. A lunar dust simulant: CLDS-i. Adv. Space Res. 59 (4), 1156–1160. https://doi.org/10.1016/j.asr.2016.11.023.

Taylor, L., Taylor, D., 2009. Living with astronomy on the moon: Mitigation of the effects of lunar crust. In: Proc. Int'l. Aeronautical Congress. CD-ROM, IAC-09 A, Daejeon, Korea.

Taylor, L., Morris, R., Pieters, C., Patchen, A., Taylor, D., Wentworth, L., McKay, D., 2000. Chemical characterization of lunar mare soils. In: Lunar and Planetary Science Conference, p. 1697.

Thompson, M.S., Zega, T.J., Becerra, P., Keane, J.T., Byrne, S., 2016. The oxidation state of nanophase Fe particles in lunar soil: implications for space weathering. Meteorit. Planet. Sci. 51 (6), 1082–1095. https://doi.org/10.1111/maps.12646.

Tompkins, S., Pieters, C.M., 2010. Spectral characteristics of lunar impact melts and inferred mineralogy. Meteorit. Planet. Sci. 45 (7), 1152–1169. https://doi.org/10.1111/j.1945-5100.2010.01074.x.

Trang, D., Lucey, P., Izenberg, N., 2015. Radiative Transfer Modeling of MESSENGER VIRS Spectra of Mercury: Detection and Mapping of Submicroscopic Iron and Carbon, Space Weathering of Airless Bodies: An Integration of Remote Sensing Data. Laboratory Experiments and Sample Analysis Workshop, p. 2043.

Vander Kaaden, K.E., McCubbin, F.M., 2015. Exotic crust formation on mercury: consequences of a shallow, FeO-poor mantle. J. Geophys. Res. Planets 120 (2), 195–209.

Zheng, Y., Wang, S., Ouyang, Z., Zou, Y., Liu, J., Li, C., Li, X., Feng, J., 2009. CAS-1 lunar soil simulant. Adv. Space Res. 43 (3), 448–454. https://doi.org/10.1016/j.asr.2008.07.006.